Phase-Resolved Wave Field Simulation Calibration of Sea Surface Reconstruction Using Noncoherent Marine Radar

YUSHENG QI, WENTING XIAO, AND DICK K. P. YUE

Department of Mechanical Engineering, Massachusetts Institute of Technology, Cambridge, Massachusetts

ABSTRACT

The possibility of reconstructing sea surface wave fields from a noncoherent X-band marine radar return has much potential for maritime operations and ocean engineering. The existing reconstruction method extracts the signal associated with gravity waves that satisfy the dispersion relationship. The process involves parameters related to how the radar signal is modulated by waves of different lengths, propagation directions, amplitudes, and phases. In the absence of independent wave measurements, these reconstruction parameters cannot be rationally adjusted according to wave field conditions, and the predictions are generally of uneven accuracy and reliability. A new reconstruction method based on concurrent phase-resolved wave field simulations is proposed. By maximizing the correlation between the reconstructed and simulated wave fields over time, optimal values of the reconstruction parameters are obtained that are found to vary appreciably with the wave field properties and with the location and size of the subdomain being sensed and reconstructed. With this phase-resolved simulation calibrated (PRSC) approach, the correlation between the evolving reconstructed wave field and that based on phase-resolved simulation, which measures the consistency and fidelity of the reconstruction, is improved significantly (by up to a factor of 2) and is obtained in a substantially broader range of sea states compared to existing methods.

1. Introduction

It has been shown that sea surface wave fields can be reconstructed from noncoherent X-band marine radar scanning a sea surface area of radius ~(2–5) km (Nieto-Borge et al. 2004; Dankert and Rosenthal 2004). The X-band radar, operating at 9.41–10.5-GHz frequency, produces Bragg back-scattered signals associated with short surface waves that are modulated by the long gravity waves of interest here. The reconstruction process involves the approximate inversion of the underlying modulation involving mainly hydrodynamic, tilt, and shadowing effects (Nieto-Borge et al. 2004; Dankert and Rosenthal 2004; Lee et al. 1995; Plant and Keller 1990).

The main approaches for radar wave reconstruction is generally based on whether the modulation is dominated by tilt modulation or shadowing modulation. The

former (see, e.g., Dankert and Rosenthal 2004) is useful for moderate radar incidence angles and is useful for relatively small radar range to height ratios. The main benefit of this approach is that in situ measurements and external calibration are not needed for scaling wave amplitude. However, for typical radars, much of the image domain is in the range where the incidence is grazing and shadowing modulation is more important than tilt modulation (Nieto-Borge et al. 2004; Lee et al. 1995; Seemann et al. 1997). In this case, the existing established method is based on Nieto-Borge et al. (2004). The basic idea here is to use three-dimensional Fourier transform on radar images (Young et al. 1985) to extract that portion of the signal associated with the gravity waves that satisfy the dispersion relationship and that correct mainly the shadowing modulation effect for the wave-related signal.

The primary focus of the present work is to explore ways to improve on the method of Nieto-Borge et al. (2004) with the use of concurrent phase-resolved wave field simulations. In the existing method, a number of empirical corrections are made to take into account the modulation of the radar signal by the waves. First, a

Corresponding author address: Dick K. P. Yue, Department of Mechanical Engineering, Massachusetts Institute of Technology, 77 Massachusetts Avenue, Cambridge, MA 02139.
E-mail: yue@mit.edu

high-pass filter is used to model the long-range distance dependence of the modulation. Second, a modulation transfer function is used to account for wave modulation effects such as shadowing. Finally, a scaling from the radar signal strength to wave amplitude is applied, generally by using the signal-to-noise ratio of the filtered signal relative to the noise in the original return to estimate the significant wave height. These processes introduce unknown empirical parameters that must be calibrated for a given radar, wave environment, and the range and azimuthal angle of the sampled subdomain relative to the radar and wave field. These calibrations require independent measurements of the wave field that are expensive and generally available for only a (small) subset of the conditions that may obtain under deployment.

To address this deficiency, we propose a new radar to the wave field reconstruction method based on concurrent phase-resolved wave field simulations. Using radar measurements over time, (nonlinear) concurrent phase-resolved wave field simulations are initialized with a set of reconstruction parameters that are adjusted and calibrated in time to maximize the consistency (measured by the phase-resolved cross correlation) between the (radar) reconstructed wave field and the simulated wave field. Since the latter contains the nonlinear phase-resolved dynamics of the waves, the optimized reconstruction parameters, which vary with (slow) time and with radar range and azimuth, provide the reconstructed wave field that best captures and represents the physical wave field. Using this approach, we are able to calibrate and optimize all of the essential parameters in the reconstruction, including those that capture the effects of modulation due to shadowing, (depth dependent) current, and nonuniformity of the radar image intensity in range and azimuth.

Using the proposed phase-resolved simulation calibrated (PRSC) approach, we find that the optimal reconstruction parameters we obtain could vary significantly depending on the location and size of reconstruction subdomain; wave conditions, such as sea state and wave frequency and directional spectra; and current. Compared with the existing reconstruction method using fixed parameters, the physical "realism" of the reconstructed wave field is significantly improved, with the correlation between the reconstructed and simulated wave field increasing by as much as a factor of 2 over a broad range of radar and wave field conditions we tested. Finally, by considering the conditions where the reconstructed-to-simulated correlation metric is high and is relatively insensitive to the reconstruction parameters, we are able to identify the regimes, in terms of sampling location and wave condition (say, wind speed),

where radar reconstruction is likely to be more accurate and robust.

The rest of paper is organized as follows. Section 2 briefly describes the existing reconstruction method. Section 3 introduces the PRSC reconstruction method. Section 4 presents the results and discussion. Summary and conclusions are given in section 5.

2. The existing standard reconstruction

We consider a radar image sequence generated from a noncoherent X-band marine radar with horizontal polarization. The image intensity represents the backscattered electromagnetic (EM) wave energy received by radar due to the Bragg resonance (Valenzuela 1978) on the sea surface between EM waves and short surface waves with wavelengths commensurate with the Bragg reflection of the X-band radar. We denote the image intensity as $\rho(\mathbf{x}, t)$ ($\mathbf{x} \in \mathscr{D}_0$), where $\mathbf{x} = (x, y)$ are horizontal coordinates, and $\mathscr{D}_0$ is the radar image scan area (with a typical radius of ~2 km).

Our objective is to reconstruct the sea surface wave elevation, denoted as $\eta(\mathbf{x}, t)$, from the radar images. The presence of surface gravity waves is manifest in the radar images due to their modulation on the shorter radar scattering waves. According to wave theory, gravity waves of frequency ω and wavenumber k satisfy a specific dispersion relationship: $\omega = \omega(k)$ and $\omega = \omega(k, \mathbf{U})$ when current $\mathbf{U}$ is present. This property distinguishes the gravity waves from other signals in the radar images. The basic idea of reconstruction is to use the dispersion relationship to extract that portion of the signal associated with the gravity waves in the frequency–wavenumber domain. This can be achieved by using three-dimensional Fourier transform to obtain radar spectra from radar images and then use the dispersion relationship to extract wave-related signal (Young et al. 1985). Because of different modulation processes in the radar and sea surface interactions, such as shadowing and tilt modulations, the separated wave-related signal must be suitably corrected to obtain the actual sea surface (Nieto-Borge et al. 2004).

The existing reconstruction method, based on the work of Young et al. (1985) and Nieto-Borge et al. (2004), includes five main steps:

1) Apply the three-dimensional fast Fourier transform (3D FFT) on radar image sequence $\rho(\mathbf{x}, t)$ to obtain its image spectrum $\tilde{\rho}(\mathbf{k}, \omega) = A_0(\mathbf{k}, \omega)e^{i\phi_0(\mathbf{k},\omega)}$, where $\mathbf{k} = (k_x, k_y)$ is the wavenumber vector.
2) Use a high-pass filter ($\omega \geq \omega_{\text{cut0}}$) and a bandpass filter [$\omega_{\text{cut1}}(\mathbf{k}) \leq \omega \leq \omega_{\text{cut2}}(\mathbf{k})$] to extract the wave-related signal from the image spectrum, obtaining the filtered

spectrum $\tilde{\rho}_f(\mathbf{k}, \omega) = A_f(\mathbf{k}, \omega)e^{i\phi_f(\mathbf{k},\omega)}$, where, for some reconstruction parameters b and c, $\omega_{\text{cut0}} = c\Delta\omega$, $\omega_{\text{cut1,2}}(\mathbf{k}) = \omega(\mathbf{k}) \pm b\Delta\omega$, and $\Delta\omega$ represent the resolved frequency of the FFT. The high-pass filter is used to eliminate low-frequency energy mainly caused by radar image long-range dependence modulation effects (Nieto-Borge et al. 2004). The bandpass filter is based on the dispersion relationship (including current $\mathbf{U}$) $\omega(\mathbf{k}, \mathbf{U})$. The empirical parameters b and c are typically assumed to be constants. The value of $\mathbf{U}$ is derived by determining the deviation between the measured dispersion relationship and the theoretical dispersion relationship (Nieto-Borge et al. 2004; Young et al. 1985).

3) Introduce a shadowing modulation correction function $M(k)$ to estimate the actual wave spectrum from the filtered spectrum $\tilde{\rho}_f(\mathbf{k}, \omega)$, obtaining the corrected wave spectrum $\tilde{\eta}_c(\mathbf{k}, \omega)$: $\tilde{\eta}_c(\mathbf{k}, \omega) = \tilde{\rho}_f(\mathbf{k}, \omega)M(k)$. Among the modulation mechanisms, except possibly for the near range, where the tilt modulation may play an appreciable role, the shadowing modulation has the dominant impact on radar imaging, especially for grazing incidence and horizontal polarization (Nieto-Borge et al. 2004; Lee et al. 1995; Seemann et al. 1997). By comparing the filtered radar spectrum and the in situ–measured buoy spectrum for select sea states, and using numerical simulation of shadowing (and tilt) modulation effects for select sea states, Nieto-Borge et al. (2004) derived an empirical form $M(k) = k^{-q}$ for the correction function, with a constant parameter q based on the mean value for the sea states they considered.

4) Apply the inverse 3D FFT on the corrected wave spectrum $\tilde{\eta}_c(\mathbf{k}, \omega)$ to obtain the unscaled elevation estimation $\eta(\mathbf{x}, t)$.

5) Obtain the actual (scaled) wave elevation $\eta_s(\mathbf{x}, t)$ from the unscaled elevation $\eta(\mathbf{x}, t)$ using an estimate of the significant wave height H_s, generally via an empirical formula based on the signal-to-noise ratio (SNR) of the filtered signal relative to the noise in the original return (Nieto-Borge 1998; Nieto-Borge et al. 2008): $H_s = c_0 + c_1\sqrt{\text{SNR}}$, where c_0 and c_1 are assumed constants (for a given installation).

Note that the filtering procedure in step 2 above is helpful in mitigating the biased and unbiased errors in the radar image data. The high-pass filter reduces the biased errors, which are more dominant in the low-frequency part of image spectrum, while the unbiased errors in the data are substantially eliminated by the bandpass filter.

To illustrate the above "standard" method, we show an example from measurements in the North Atlantic

TABLE 1. Physical parameters associated with the radar image sequence example in section 2, which has a radius of $\sim$2 km (544 $\times$ 544 grids in one frame with a grid distance of 7.5 m) and a sequence duration of 48 s with a time interval of 1.5 s between frames (OceanWaves GmbH 2008). The radar height is $\sim$36 m.

Location	$\sim$39.2°N, 73.2°W
Date	15 Aug 2006
Water depth	85 m
Wind speed	10.6 m s^{-1}
Wind direction	213°

Ocean using a commercial noncoherent X-band marine radar (OceanWaves GmbH 2008). The associated physical parameters, provided by OceanWaves (GmbH 2008), are shown in Table 1. Figure 1a shows one frame of the raw radar image $\rho(\mathbf{x}, t = t_0)$ of radius R. For reconstruction, we choose some subdomain $\mathscr{D}_1$ where there is appreciable signal in the radar image sequence. For convenience, we select a square subdomain (aligned with the Cartesian coordinates) characterized by (normalized) length $L/R = s$, and center azimuthal coordinate α and (normalized) range $D/R = d$. In the example in Fig. 1, we set $\alpha = 90°$, which is close to the downwind direction, and $d = 0.5$ and $s = 0.5$. Figure 1b shows the details of the radar signal ρ in $\mathscr{D}_1$. Note that the signal becomes weaker with increasing radar range. Figure 1c shows the magnitude of image spectrum $|\tilde{\rho}|(k, \omega)$ with $k = (k_x^2 + k_y^2)^{1/2}$, after the 3D FFT of Fig. 1b. The somewhat stronger signal is scattered in a band around the dispersion curve $\omega \sim \sqrt{gk}$ (this will be shifted in the presence of significant current). There is also significant return at low frequency spread across k. Figure 1d shows $|\tilde{\rho}_f|(k, \omega)$ after bandpass filtering (with $b = 1$) around the dispersion curve and high-pass filtering (with $c = 2$). Finally, the filtered spectrum $\tilde{\rho}_f$ is corrected for shadowing by the modulation correction function $M(k)$ (with $q = 1.2$; Nieto-Borge et al. 2004) to obtain $\tilde{\eta}_c$ [Fig. 1e, which shows the comparison of the normalized one-dimensional spectra $S(\omega)$ of $\tilde{\rho}_f$ and $\tilde{\eta}_c$]. Figure 1f plots one frame of the unscaled elevation estimation $\eta(\mathbf{x}, t = t_0)$ after the inverse FFT of $\tilde{\eta}_c$. The scaled reconstructed wave field $\eta_s(\mathbf{x}, t)$ is now obtained by scaling $\eta(\mathbf{x}, t)$ by a constant factor to obtain a given H_s for η_s. The value of H_s is obtained from the SNR relating the (integrated) signal $\tilde{\rho}_f$ to noise $\tilde{\rho} - \tilde{\rho}_f$ (in this case, SNR $\approx$ 2.8 from Figs. 1c and 1d).

The standard method above involves empirical reconstruction parameters, notably the filtering parameters b and c; the shadowing correction parameter q; and the SNR to H_s scaling coefficients c_0 and c_1. For a given radar deployment, the parameters c, c_0, and c_1 are not expected to vary too significantly for different wave conditions. On the other hand, the bandpass parameter
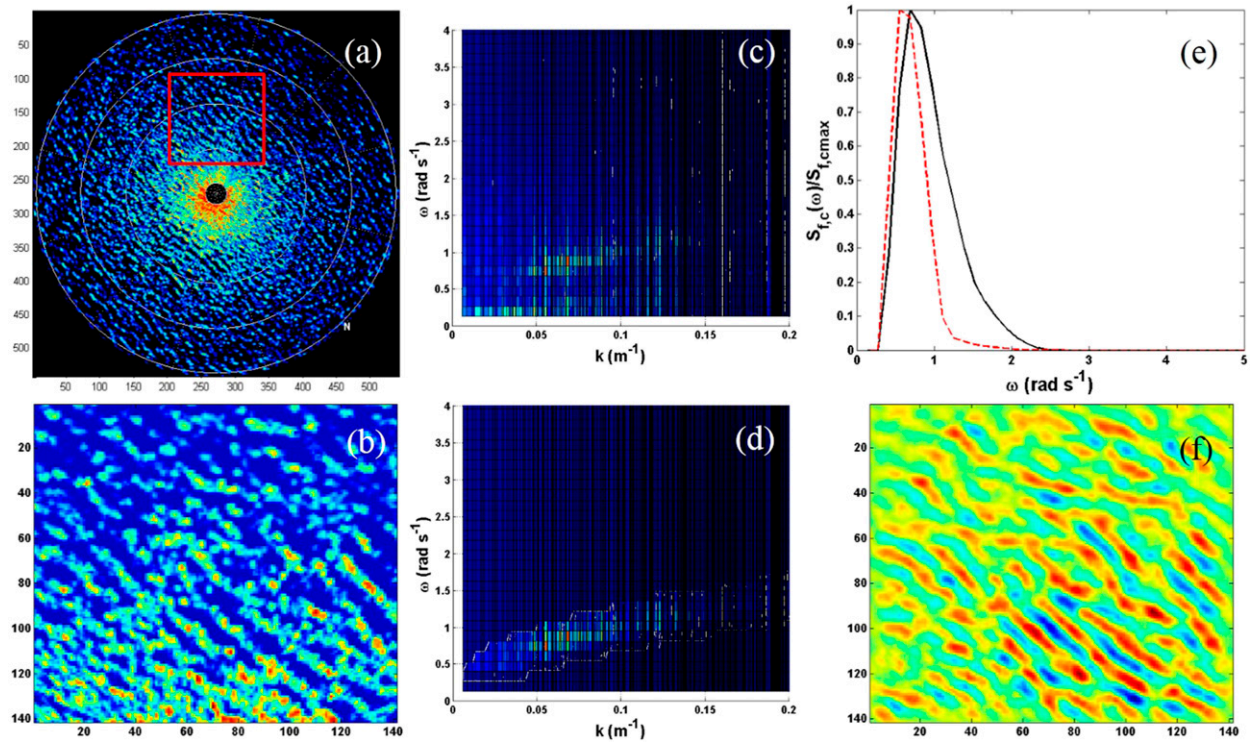
FIG. 1. (a) One frame of the raw radar image sequence $\rho(\mathbf{x}, t = t_0)$ (data provided by OceanWaves GmbH 2008), where the colors indicate the strength of radar image intensity (red: high intensity; blue: low intensity), the red square shows $\mathscr{D}_1$, and the axes labels represent grid number. (b) Radar signal in $\mathscr{D}_1$, where the axes labels represent the grid number. (c) Magnitude of the image spectrum $|\tilde{\rho}|(k, \omega)$, where the colors indicate the spectrum magnitude (red: large magnitude; blue: small magnitude). (d) Magnitude of the filtered spectrum $|\tilde{\rho}_f|(k, \omega)$. (e) Normalized one-dimensional spectra $S(\omega)$ of the filtered spectrum $\tilde{\rho}_f$ (black line) and corrected spectrum $\tilde{\eta}_c$ (red dashed line). (f) One frame of unscaled elevation estimation $\eta(\mathbf{x}, t = t_0)$, where the colors indicate the surface elevation (red: high elevation; blue: low elevation).

b and the shadowing correction parameter q depend on the specifics of the wave field relative to the radar, and hence are also functions of azimuth angle α and range parameter d (and also subdomain size parameter s).

Finally, when a (uniform) current $\mathbf{U}$ is present, it can, in principle, be obtained from the radar image spectrum $\tilde{\rho}(\mathbf{k}, \omega)$ by a shift of $\omega(\mathbf{k}, \mathbf{U}) = \omega_0(\mathbf{k}) + \mathbf{k} \cdot \mathbf{U}$, where $\omega_0(\mathbf{k})$ corresponds to the theoretical dispersion relationship. This is not weighted by the wavenumbers of the significant (propagating) waves, and the best-fit shift may not obtain a good estimate of $\mathbf{U}$. In the (common) situation when the current is vertically sheared, the effect of $\mathbf{U}(z)$ on the wave phase speed is wavenumber dependent, and the standard method is even less likely to obtain a good estimate of $\mathbf{U}$.

3. New PRSC reconstruction method

We propose a new PRSC approach wherein the reconstruction parameters are calibrated by comparing the reconstructed wave field with concurrent phase-resolved simulations that capture the (nonlinear) gravity wave dynamics. Furthermore, the effect of (sheared)

current can be incorporated into the wave simulations in a straightforward way to provide a calibrated best fit to the radar data. For a given set of reconstruction (and current) parameters Π and a set of radar return images $\rho(\mathbf{x}, t)$, a set of reconstructed wave fields $\eta_\Pi(\mathbf{x}, t)$ can be reconstructed using the standard approach illustrated above. At the same time, phase-resolved wave fields $\zeta_\Pi(\mathbf{x}, t)$, initialized by η_Π, are obtained by direct simulation. The parameters Π can be optimized by phase-resolved comparisons of η_Π and ζ_Π (for simplicity, the subscripts Π are omitted hereafter without ambiguity) at later time τ. Specifically, we seek Π to maximize the correlation between η and ζ defined by the normalized cross-correlation coefficient, which is used to measure the consistency and fidelity of the wave field reconstruction:

$$\text{Cor}(\tau) = \frac{\sum_{\mathbf{x}} [\eta(\mathbf{x}, t_0 + \tau) - \overline{\eta}][\zeta(\mathbf{x}, t_0 + \tau) - \overline{\zeta}]}{\left\{ \sum_{\mathbf{x}} [\eta(\mathbf{x}, t_0 + \tau) - \overline{\eta}]^2 \sum_{\mathbf{x}} [\zeta(\mathbf{x}, t_0 + \tau) - \overline{\zeta}]^2 \right\}^{1/2}},$$

$$(1)$$

where t_0 is an initial time and $\overline{\eta}$ and $\overline{\zeta}$ represent the average over the sampled spatial domain ($\mathscr{D}_1$).

The specific simulation model used to provide the concurrent phase-resolved wave field is not critical. However, there are a number of important considerations: 1) the simulation model needs to be capable of simulating phase-resolved (long) waves in a typical radar field size [say, $O(\text{km})^2$]; 2) the simulations must be highly computationally efficient to allow for multiparameter optimization of the wave field reconstruction [typically requiring $\gtrsim O(10)$ concurrent simulations]; and 3) depending on the location and application, it may be important for the model to account for steep waves, (depth varying) current, and finite depth with varying bathymetry.

To satisfy these requirements, we use a phase-resolved simulation model based on a high-order spectral (HOS) method (Mei et al. 2005). For nonlinear gravity waves in the context of potential flow, the HOS method can efficiently simulate the evolution of wave elevation in a large domain [$\sim O(10\,\text{km})^2$], accounting for the evolution of large numbers N [$\gtrsim O(10^3)$ per dimension] of wave modes and accounting for their nonlinear interactions up to an arbitrary order of M in wave steepness. The methods obtain exponential convergence with N and M, and have a computation count linearly proportional to N and M (Dommermuth and Yue 1987). HOS has been extended to account for finite depth, varying bottom topography, current, and density stratification (Mei et al. 2005; Liu and Yue 1998; Dommermuth and Yue 1988; Alam et al. 2009). In general, it can handle depth-dependent current directly in the free-surface dynamic boundary condition (Mei et al. 2005). Hereafter, we typically use HOS with $N = 32^2$ in the reconstruction subdomain and $M = 3$ (to include the leading effect of nonlinearity on wave group velocity).

To understand the behavior of $\text{Cor}(\tau)$ when the reconstructed wave field is close to an actual wave field, we use the JONSWAP directional spectrum (Hasselmann et al. 1973) (using the same range of wavenumbers as in our radar image example) to generate a synthetic wave field $\eta(\mathbf{x}, t)$ in a large domain $\mathscr{D}_0$ (of radius 2 km). We conduct an HOS simulation in $\mathscr{D}_1$ (of size $1\,\text{km}^2$, the same as the square window in Fig. 1a), starting with initial condition $\zeta(\mathbf{x}, t_0) = \eta(\mathbf{x}, t_0)$. Figure 2 plots typical time histories of $\text{Cor}(\tau)$ between $\eta(\mathbf{x}, t_0 + \tau)$ and $\zeta(\mathbf{x}, t_0 + \tau)$. For a given $\mathscr{D}_1$ relative to $\mathscr{D}_0$, $\text{Cor}(\tau)$ decreases (slowly) with τ, as expected (e.g., by $\sim$10% for $\tau/T_p \sim 3$, for the wave parameters in Fig. 2). The reduction in $\text{Cor}(\tau)$ with τ reflects the devolution of the wave field in $\mathscr{D}_1$ with (slow) time as waves (captured in the bigger domain $\mathscr{D}_0$) enter and leave this subdomain. This is elucidated in Fig. 3,
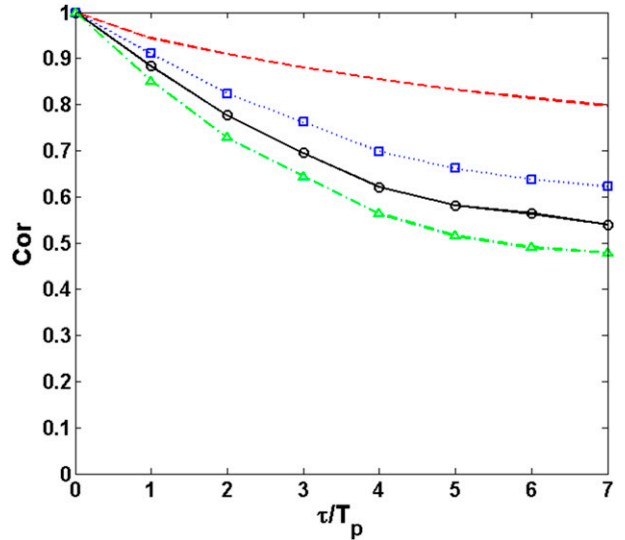

FIG. 2. Time histories of $\text{Cor}(\tau)$ for: the synthetic wave field based on a JONSWAP spectrum for peak enhancement factor $\gamma = 3.3$, spreading angle $\Theta = 60°$, and wave steepness $\varepsilon = 0.15$) (red dashed line); radar image sample in $\mathscr{D}_1$ in Fig. 1 using the standard reconstruction method with fixed reconstruction parameters (black line with circle); radar image sample in $\mathscr{D}_1$ in Fig. 1 using the standard method but with reconstruction parameter $q = 0.5$ (blue dotted line with square); and radar image sample in a different sampling azimuthal position $\alpha = 315°$ in Fig. 1 using the standard method with fixed parameters (green dashed–dotted line with triangles).

which shows the point-to-point error $|\eta(\mathbf{x}, t) - \zeta(\mathbf{x}, t)|$ in $\mathscr{D}_1$ at different times.

The decorrelation with time is also seen in Fig. 2 for real radar data in the example in Fig. 1, where the standard reconstruction method with fixed parameters Π is applied. The decrease with τ is faster than that for the synthetic JONSWAP case because the radar image and reconstruction are not able to capture all the necessary wave information or the true information (especially in the reconstructed wave field). The effect of the former is seen when the azimuthal position of $\mathscr{D}_1$ is changed from close to downwind $\alpha = 90°$ (in Fig. 1) to almost crosswind $\alpha = 315°$, where the radar image is of poorer quality. The effect of the latter is underscored when an appreciably higher correlation is obtained with optimized reconstruction parameter $q = 0.5$ rather than the original value of $q = 1.2$ (Nieto-Borge et al. 2004). In general, the optimal reconstruction parameter Π are function of both the wave field and the radar sampling subdomain. Figure 2 illustrates the key idea of the PRSC approach, wherein Π (for a given wave condition and $\mathscr{D}_1$) are optimized by maximizing $\text{Cor}(\tau)$. Based on results such as those in Fig. 2, we typically use $\tau/T_p = 3$ in Eq. (1). The reconstruction parameters and wave
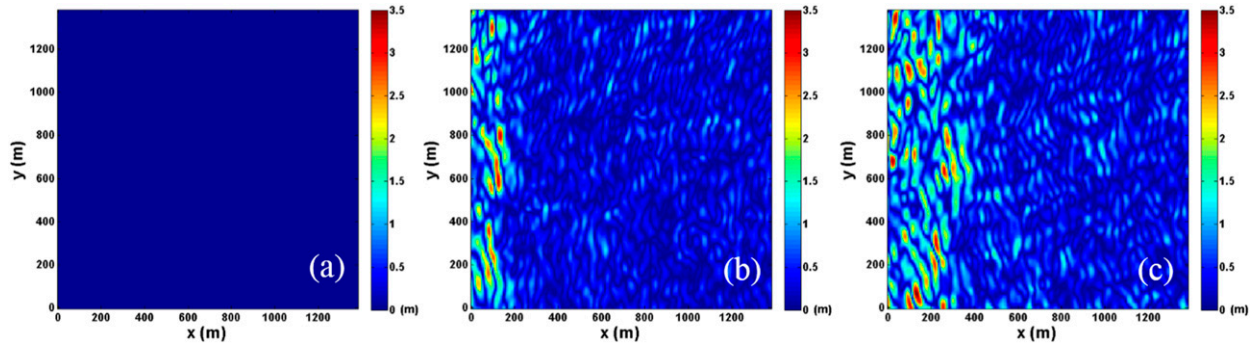
FIG. 3. Point-to-point absolute error (m) between actual and simulated waves $|\eta(\mathbf{x}, t) - \zeta(\mathbf{x}, t)|$ in $\mathcal{D}_1$ at different evolution times $\tau/T_p =$ (a) 0, (b) 3, and (c) 6, for a synthetic wave field based on the JONSWAP spectrum with peak enhancement factor $\gamma = 3.3$, spreading angle $\Theta = 60°$, and wave steepness $\varepsilon = 0.15$. Main wave propagation direction is from left to right.

field predictions turn out not to be sensitive to the specific value of τ around this choice. For example, in all the cases we consider here, optimized reconstruction parameters vary within $O(1\%)$ when τ/T_p is varied between 2 and 5.

Now we consider a radar image sequence $\rho_0(\mathbf{x}, t)$ obtained by a noncoherent X-band marine radar (e.g., Fig. 1a) covering $\mathcal{D}_0$. Consider a sample radar image $\rho(\mathbf{x}, t)$ in $\mathcal{D}_1$ where there is an appreciable signal. The location and size of the sample is represented by α, d, and s (see Fig. 1). Our objective is to reconstruct sea surface elevation $\eta(\mathbf{x}, t)$ in $\mathcal{D}_1$ using the radar image $\rho(\mathbf{x}, t)$.

The PRSC reconstruction method uses the correlation $\mathrm{Cor}(\tau)$ between the reconstructed wave field η and concurrent phase-resolved simulations ζ as a metric to measure the consistency and fidelity of reconstruction. For a given radar image sample $\rho(\mathbf{x}, t)$ and Π, we obtain reconstructed wave fields $\eta_\Pi(\mathbf{x}, t)$ and concurrent phase-resolved simulations $\zeta_\Pi(\mathbf{x}, t > t_0)$, initialized by $\eta_\Pi(t_0)$, so that we can calculate their correlation $\mathrm{Cor}(\tau)$ using Eq. (1). For simplicity, we denote $\chi = \mathrm{Cor}(\tau = 3T_p)$ as the reconstruction fidelity index. Once χ is obtained, we maximize χ over the values of Π using the standard optimizing scheme (e.g., the simple gradient method) to obtain the optimal values of Π^*, which is a function of the radar image sample location (α, d) and size s, and the properties of the wave field in question. Given $\rho(\mathbf{x}, t)$ and Π, the reconstructed wave field evolution $\eta_\Pi(\mathbf{x}, t)$ required to calculate χ is obtained as follows:

(i) Radar image calibration. The radar image intensity has generally a notable range and direction dependence manifest in the raw images $\rho(\mathbf{x}, t)$ as well as in its frequency–wavenumber spectrum $\tilde{\rho}(\mathbf{k}, \omega)$ (notably in the energy in the low frequency). We put forward a radar image intensity calibration to correct for the range and direction dependence, with a calibrated radar image intensity given by

$$\rho_c(r, \alpha, t) = C(r, \alpha)\rho(r, \alpha, t), \tag{2}$$

where r and α are the radial and azimuthal coordinates, respectively; and $C(r, \alpha)$ is a calibration function involving two reconstruction parameters δ and ν that are to be optimized [see section 3a(1)].

(ii) 3D FFT. Similar to the standard method, we apply the 3D FFT to $\rho_c(\mathbf{x}, t)$ to get the image spectrum $\tilde{\rho}(\mathbf{k}, \omega)$, which has magnitude $A_0(\mathbf{k}, \omega)$ and phase $\phi_0(\mathbf{k}, \omega)$ of $\tilde{\rho}(\mathbf{k}, \omega) = A_0(\mathbf{k}, \omega)e^{i\phi_0(\mathbf{k}, \omega)}$.

(iii) Filter. Similar to the standard method, we use a high-pass filter (with parameter c) and bandpass filter (with parameter b) to extract the wave-related signal from the image spectrum, obtaining the filtered spectrum $\tilde{\rho}_f(\mathbf{k}, \omega) = A_f(\mathbf{k}, \omega)e^{i\phi_f(\mathbf{k}, \omega)}$. The bandpass filter is based on the wave dispersion relationship. For gravity waves with finite and constant water depth (H), the dispersion relationship, taking current (constant $\mathbf{U}$ relative to radar) into account, is

$$\omega(\mathbf{k}, \mathbf{U}) = \omega_0(\mathbf{k}) + \mathbf{k} \cdot \mathbf{U} = \sqrt{gk\tanh kH} + \mathbf{k} \cdot \mathbf{U}, \tag{3}$$

where the current $\mathbf{U}$ is obtained in the standard method by determining the deviation between the measured dispersion relation and the theoretical dispersion relation (Young et al. 1985; Nieto-Borge et al. 2004). For the PRSC method, we optimize the value of $\mathbf{U}$ by maximizing χ [see section 3a(2)]. Nieto Borge et al. proposed a fixed value $b = 1$ in the bandpass filter cutoff frequency $\omega_{\mathrm{cut}1,2}(\mathbf{k}) = \omega(\mathbf{k}) \pm b\Delta\omega$ (Nieto-Borge et al. 2004). In the PRSC method, we allow b to be optimized in the range [1,3]. The value of c is usually an integer for discrete FFT and is found to not vary significantly for different wave conditions. We fix $c = 2$, which is enough to eliminate the low-frequency energy

caused by radar image long-range dependence modulation effects without affecting the wave-related signal in the radar image spectrum.

(iv) Correction. To estimate the actual wave spectrum, we use a shadowing modulation correction function $M(k)$ to correct the magnitude A_f, given by

$$A_c(\mathbf{k}, \omega) = A_f(\mathbf{k}, \omega) M(k), \tag{4}$$

where $k = |\mathbf{k}|$ and to obtain the corrected wave spectrum: $\tilde{\eta}_c(\mathbf{k}, \omega) = A_c(\mathbf{k}, \omega) e^{i\phi_f(\mathbf{k}, \omega)}$. We use the same shadowing correction function form $M(k) = k^{-q}$ as in the standard method, but the correction parameter q is not fixed and is optimized in the PRSC scheme depending on the wave field and the location of $\mathscr{D}_1$ [see section 3a(3)].

(v) Inverse 3D FFT. Apply the inverse 3D FFT on the corrected wave spectrum $\tilde{\eta}_c(\mathbf{k}, \omega)$ to obtain the unscaled elevation $\eta(\mathbf{x}, t)$.

Finally, the elevation $\eta(\mathbf{x}, t)$ must be scaled to represent the actual wave elevation. For a given radar, the scaling based on the SNR in the radar return appears to be robust (Alpers and Hasselmann 1982; Plant and Zurk 1997; Ziemer and Günther 1994; Nieto-Borge 1998; Nieto-Borge et al. 2008). In principle, since the wave dispersion is affected by the wave amplitude, the PRSC method using nonlinear simulation can provide an independent scaling calibration. This is the subject of ongoing research.

Key reconstruction parameters

1) RADAR IMAGE CALIBRATION PARAMETERS

Radar image intensity has range and direction dependence. Figure 1a shows one frame of raw radar image that we can represent as $\rho(r, \alpha)$, where r and α are radial and azimuthal coordinates, respectively. We denote the direction-averaged radar image intensity as

$$\rho(r) \equiv \frac{1}{2\pi} \int_0^{2\pi} \rho(r, \alpha) \, d\alpha$$

and the range-averaged radar image intensity as

$$\rho(\alpha) \equiv \frac{1}{R - r_0} \int_{r_0}^{R} \rho(r, \alpha) \, dr,$$

where R and r_0 are the maximum and minimum radii of the radar image, respectively.

For the radar data used in Fig. 1a, Fig. 4 shows the normalized direction-averaged and range-averaged radar image intensity. It is clear that radar image intensity decreases with increasing range. The ratio of the maximum image intensity and the minimum image intensity

is about $O(10)$. And we can see that the radar image intensity has a peak near the upwind direction ($\alpha_w = 213°$) and drops about 60% around the downwind direction. Typical of noncoherent radar return as shown in Fig. 4, the radar image intensity generally decreases with increasing range r or increasing direction deviation $|\alpha - \alpha_w|$ from the upwind direction.

This nonuniformity of radar image intensity as a function of range and azimuth must be accounted for in the wave field reconstruction. To do this, we use a calibration function $C(r, \alpha)$ to calibrate the radar image intensity: $\rho_c(r, \alpha, t) = C(r, \alpha)\rho_s(r, \alpha, t)$. For simplicity, we separate the range and direction dependence effects, and write the calibration function as

$$C(r, \alpha) = f_1(r) f_2(|\alpha - \alpha_w|), \tag{5}$$

where $C(r, \alpha)$ should be a monotonically increasing function of r and $|\alpha - \alpha_w|$ with f_1 and f_2 used to account for the range and direction dependence effects, respectively.

Figure 4a also shows that the radar image intensity decreases dramatically within $r/R \leq 0.5$, while it decreases slowly for $r/R > 0.5$. Thus, we propose a simple form for $f_1(r)$:

$$f_1(r) = \begin{cases} (r/R)^\delta, & d \leq 0.5 \\ 1, & d > 0.5 \end{cases}, \tag{6}$$

where d is the normalized range of the radar image sample center, $\delta \geq 0$ is a parameter to be determined, and $\delta = 0$ for $d > 0.5$ 0.

From Fig. 4b we can see that around the upwind direction ($\alpha \approx \alpha_w$), the radar image intensity does not change much; thus, we propose a simple form for $f_2(|\alpha - \alpha_w|)$:

$$\begin{aligned} f_2(|\alpha - \alpha_w|) &= 1 + \nu[1 - \cos(|\alpha - \alpha_w|)] \\ &= 1 + \nu[1 - \cos(\alpha - \alpha_w)], \end{aligned} \tag{7}$$

where $\nu \geq 0$ is a parameter to be determined. This function has properties that equal 1 when $\alpha = \alpha_w$ and they increase monotonically with increasing $|\alpha - \alpha_w|$ in the range of $[0, \pi]$.

For a different radar image sample location, the calibration parameter δ and ν vary and are optimized by maximizing χ.

2) ACCOUNTING FOR CURRENT

In the PRSC method, the current ($\mathbf{U}$) is taken into account directly in (the free-surface dynamic boundary condition of) the HOS simulations (Mei et al. 2005), and the optimization process to maximize χ obtains the magnitude and direction (and possibly depth dependence) of
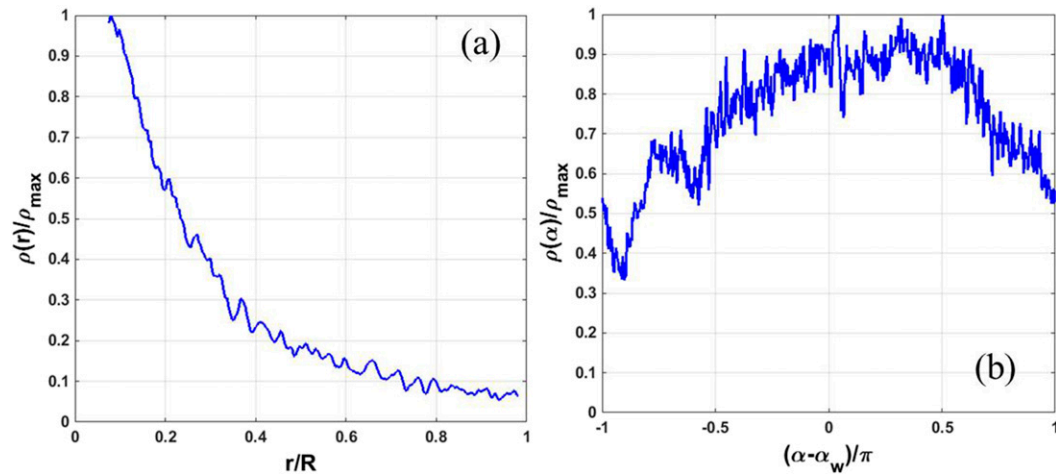
FIG. 4. (a) Range dependence of normalized radar image intensity $\rho(r)/\rho_{max}$, where R is the maximum range in the radar images and r/R is the normalized range. (b) Direction dependence of normalized radar image intensity $\rho(\alpha)/\rho_{max}$, where α is the azimuthal coordinate and α_w is the upwind direction. Raw radar data are provided by OceanWaves GmbH (2008).

U that best fits the observed radar signal. Thus, **U** is formally a component of Π. Figure 5 compares the performance of the reconstruction using the PRSC optimized current versus that obtained in a standard method using a least squares fit of the dispersion relationship [Eq. (3)]. For this particular dataset, the difference between the PRSC method and standard method predictions of **U** is ~35%, with corresponding χ values of 0.65 and 0.38, respectively.

3) SHADOWING CORRECTION PARAMETER

A key step in the standard reconstruction method is the wavenumber spectral correction $M(k)$ to account for (mainly) the wave shadowing effect (Nieto-Borge et al. 2004). To illustrate this shadowing effect, consider a given (phase resolved) wave field $\zeta(x, y, t)$ and the corresponding radar-illuminated field $\zeta_-(x, y, t)$, depending on the radar height h, where regions of ζ blocked from direct radar line of sight are zeroed out. Figure 6 shows the instantaneous $\zeta(x, y, t)$ and $\zeta_-(x, y, t)$. From Fig. 6b we can see that the shadowing modulation is weaker for smaller range and in the cross-wave regions. Also plotted are the corresponding normalized frequency spectra $\tilde{\zeta}(\omega)/\tilde{\zeta}_{max}$ and $\tilde{\zeta}_-(\omega)/\tilde{\zeta}_{-,max}$ integrated over the sampling $\mathscr{D}_1$. Note that, comparing the two spectra, we see the net effect of wave shadowing therefore is manifest as a shift of $\tilde{\zeta}(\omega)$ toward higher frequency. This shift can be approximated by $\tilde{\zeta}(\omega) \approx M(\omega)\tilde{\zeta}_-(\omega)$, where $M(\omega) = \omega^{-p}$, or $M(k) = k^{-q}$, where, for deep water, $q = p/2$ from the dispersion relationship. Figure 6d plots $\ln(M)$ with respect to $\ln(\omega)$, from which we see that they approximately satisfy a linear relationship with slope p.

Figure 7 plots values of the shadowing correction function exponent p obtained from different $\mathscr{D}_1$ and for phase-resolved wave fields with different H_s. In general, p varies depending on the range and the relative azimuth of the subdomain and with H_s/h. Figure 7a shows that the shadowing modulation parameter p has a somewhat lower value for smaller d, corresponding to the weaker
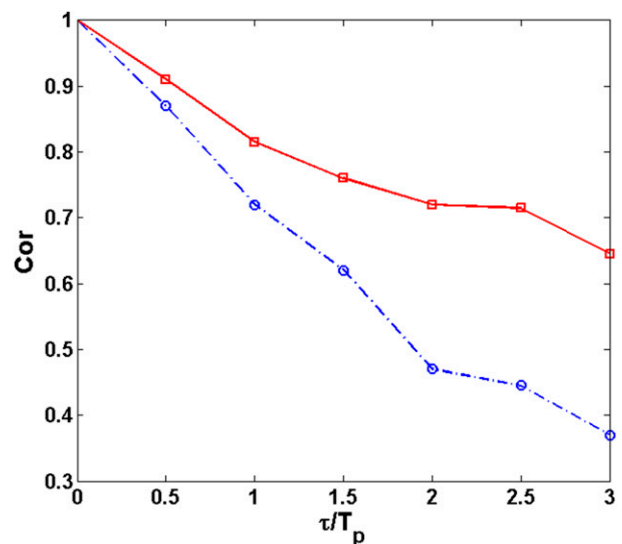

FIG. 5. Time histories of Cor (τ) for wave field reconstructed using current values obtained from the PRSC optimization (red line with squares) vs that from the standard method (blue dashed–dotted line with circles). The PRSC optimized current is given by $|\mathbf{U}| = 0.89 \, \mathrm{m \, s^{-1}}$ with azimuth $\theta_U = 341°$, while the standard method has best-fit values [from Eq. (3)] of $|\mathbf{U}| = 0.66 \, \mathrm{m \, s^{-1}}$ and $\theta_U = 337°$. Radar data are from the North Atlantic, 10 Sep 2007 (OceanWaves GmbH 2008).
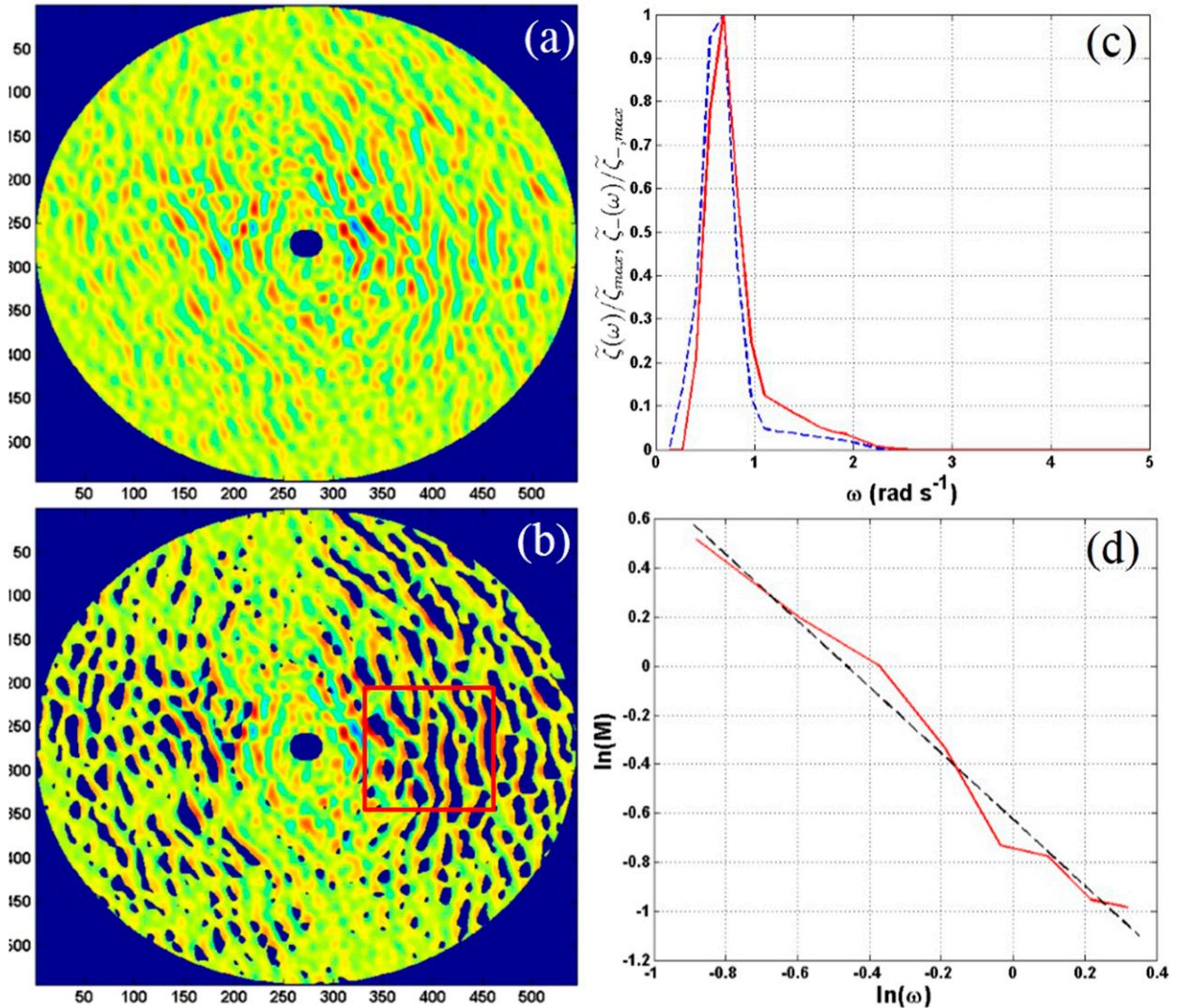
FIG. 6. (a) Synthetic wave field ζ in a 2-km-radius circle generated from a JONSWAP spectrum with $H_s = 5.8$ m propagating mainly from left to right, and where the axes labels represent a grid number with a grid interval of 7.5 m. (b) Instantaneous radar-illuminated field ζ_-, with a radar height of 36 m, where the red square represents $\mathscr{D}_1$. (c) Normalized frequency spectra $\tilde{\zeta}(\omega)/\tilde{\zeta}_{max}$ (blue dashed line) and $\tilde{\zeta}_-(\omega)/\tilde{\zeta}_{-,max}$ (red line) in $\mathscr{D}_1$. (d) Relationship between $\ln(M)$ and $\ln(\omega)$ (red line) and the data trend (black dashed line).

shadowing modulation in the nearer field (see Fig. 6b). For very large d (closer to 1), the value of p again decreases, reflecting the fact that with increasingly greater shadowing, the wave information contained in the radar return is eventually also obscured. As expected, p is generally greater for α close to the upwind or downwind direction, and it generally increases with increasing H_s/h. Dependencies of p on other wave field parameters, such as direction spread and peak frequency, are similarly found.

4. Results and discussion

The variations of the optimal reconstruction parameters and the resultant fidelity of the reconstructed wave field depend on the reconstruction subdomain in the radar image, as well as the actual wave field conditions. We discuss these in sequence in the following.

a. Dependence on reconstruction subdomain location and size

We first consider the sensitivity of the reconstruction parameters to the location and size of $\mathscr{D}_1$ in the overall radar image. As a specific example, we return to the radar measurement in section 2 (see Table 1).

For the fixed $\mathscr{D}_1$ in Fig. 1 corresponding to $\alpha = 90°$, $d = 0.5$, and $s = 0.5$, the results using the standard method with fixed reconstruction parameters $q = 1.2$, $b = 1$, and $\delta = \nu = 0$ yield a fidelity index of $\chi = 0.69$.
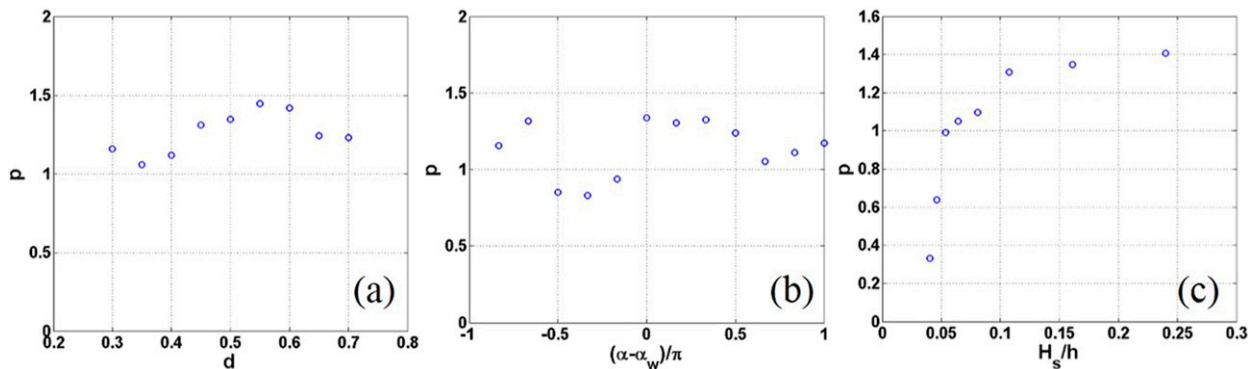
FIG. 7. Variation of shadowing correction function exponent $p = 2q$ with respect to (a) d ($\alpha = \alpha_w$ and $H_s/h = 0.16$), (b) α ($d = 0.5$ and $H_s/h = 0.16$), and (c) H_s/h ($h = 36$ m, $d = 0.5$, and $\alpha = \alpha_w$).

Using the PRSC method, we obtain optimized parameters corresponding to $q = 0.5$, $b = 1.8$, and $\delta = \nu = 0$, which yield $\chi = 0.76$.

The results are sensitive to the location and size of $\mathscr{D}_1$. Figure 8 plots the optimized PRSC reconstruction parameters q^*, δ^*, and ν^* as functions of subdomain azimuth α, range d, and size s. The variations of the optimized parameters with α, d, and s underscore the advantage of reconstruction using nonconstant (optimized) parameters.

The shadowing correction parameter q is one of the key parameters in the radar reconstruction. Figure 8a shows a distinct variation of the optimized q^* with α relative to the wind direction α_w, with significant differences in the value of q^* when $\mathscr{D}_1$ is upwind–downwind direction versus in the crosswind direction, $\alpha \approx \alpha_w \pm \pi/2$. This reflects the effect of shadowing modulation, which is weaker in the cross-wave directions (see Fig. 6b). The dependence of q^* on d (Fig. 8b) also reflects the increasing strength of shadowing modulation with range (see Fig. 6b), with q^* appearing to reach an asymptotic optimal value for greater

d (approaching 1). The size of the reconstruction subdomain s also has a distinct effect on q^* with a monotonic decrease of the value of q^* with increasing s (see Fig. 8c). In this case, $\mathscr{D}_1$ is centered at $d = 0.5$, near the "sweet spot" for shadowing modulation (see Fig. 7a). As s increases, $\mathscr{D}_1$ is no longer focused in this region and (optimal) q^* must be adjusted accordingly.

The value of δ^* is near 0 for all α in the case of $d = 0.5$ (Fig. 8a), which is consistent with the calibration function $f_1(r) = 1$ for $d > 0.5$. The variation of δ^* with respect to d is shown in Fig. 8b. We see that δ^* gradually decreases with increasing d and that $\delta^* \approx 0$ for $d \geq 0.5$. More specifically, Fig. 9a shows the variation of χ with respect to δ for different d with other factors fixed. We can see that the proposed radar image calibration method is helpful in improving the reconstruction fidelity when d is small ($d < 0.5$). This is reasonable in the sense that the nonuniformity of the radar image intensity is more notable in a smaller range.

The variation of ν^* with respect to α is shown in Fig. 8a. We see that around the upwind or downwind direction $\nu^* = 0$, while around the crosswind direction
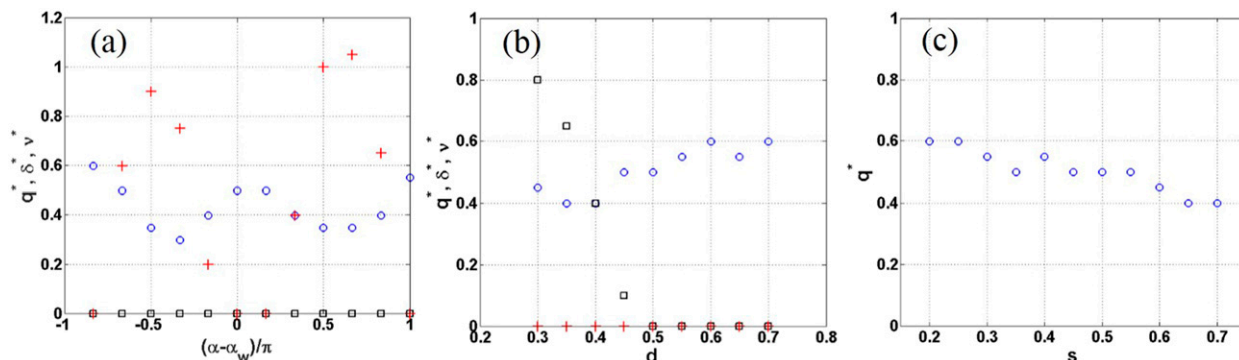

FIG. 8. Variation of optimized PRSC reconstruction parameters q^* (blue circles), δ^* (black squares), and ν^* (red plus signs) with respect to (a) α (upwind direction $\alpha_w = 213°$, $d = 0.5$, $s = 0.5$), (b) d ($\alpha = \alpha_w$, $s = 0.5$), and (c) s ($\alpha = \alpha_w$, $d = 0.5$). Note that for (c), the optimized δ^* and ν^* are both approximately 0 for all s. The standard method corresponds to fixed $q = 1.2$ and $\delta = \nu = 0$.
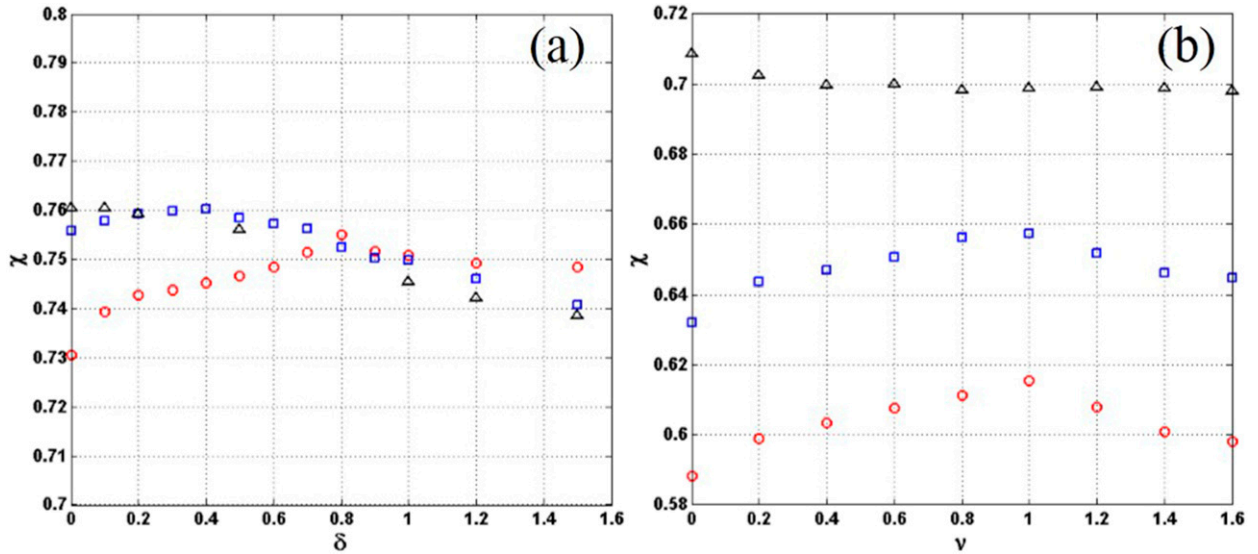
FIG. 9. Variation of χ with respect to reconstruction parameters (a) δ for $d = 0.3$ (red circles), 0.4 (blue squares), and 0.5 (black triangles), with $\alpha = \alpha_w$, $s = 0.5$, $\nu = 0$, $q = 0.5$, and $b = 1.8$; and (b) ν for $\alpha - \alpha_w = -\pi/2$ (red circles), $\alpha - \alpha_w = \pi/2$ (blue squares), $\alpha - \alpha_w = \pi$ (black triangles), with $d = 0.5$, $s = 0.5$, $\delta = 0$, $q = 0.5$, and $b = 1.8$.

ν^* has significant nonzero values. Thus, in the case of $\alpha = \alpha_w$ (Fig. 8b), $\nu^* = 0$ for different d. More specifically, Fig. 9b shows the variation of χ with respect to ν for different α with other factors fixed. We can see that if we choose $\mathscr{D}_1$ in the upwind or downwind direction, $\nu^* = 0$ and the calibration function $f_2(\alpha) = 1$, which means no calibration with respect to the azimuth is needed in these regions. However, if we choose $\mathscr{D}_1$ in directions close to the crosswind direction, this calibration function helps to improve the fidelity of reconstruction by $\sim5\%$ with ν^*. Terms δ^* and ν^* are found to be insensitive to s, so the variations of δ^* and ν^* with respect to s are not shown here.

Clearly, using constant (or averaged) values for these parameters would be suboptimal. Note that reconstruction parameter b is found to be only weakly dependent on the choice of the reconstruction subdomain, and the variation of b with respect to α, d, and s is not shown here.

Figure 10 plots the reconstruction fidelity indices χ obtained using fixed parameters Π_0 in the standard approach versus those obtained from PRSC reconstruction with optimized parameters Π^* for different locations and sizes of $\mathscr{D}_1$. We see that the PRSC method can increase χ by $\sim(0.1-0.2)$ compared to the standard method for different locations and sizes of $\mathscr{D}_1$ of the radar image sequence under consideration. Using the PRSC method, the resultant χ is uniformly high [$\sim(0.7-0.8)$] for different $\mathscr{D}_1$, while using the standard method, the resultant χ varies significantly in a range [$\sim(0.5-0.7)$] with respect to α, d, and s.
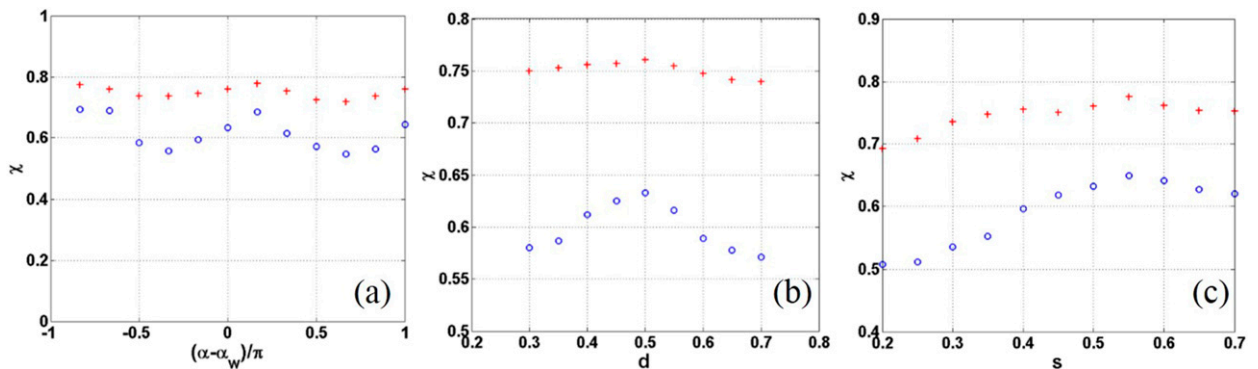

FIG. 10. Variation of χ with respect to (a) α, (b) d, and (c) s, using the standard reconstruction method (blue circles) with fixed parameters Π_0 ($q = 1.2$, $\delta = 0$, $\nu = 0$, $b = 1$) and the PRSC method (red plus signs) with optimized parameters Π^*. When not varied, the location and size of $\mathscr{D}_1$ are set to $\alpha = \alpha_w$, $d = 0.5$, and $s = 0.5$.

TABLE 2. As in Table 1, but for the 15 sets of the radar image sequence in section 4b.

Location	~39.2°N, 73.2°W
Date	Aug ~ Sep 2006
Water depth	77–100 m
Wind speed	5–22 m s^{-1}

Specifically, Fig. 10a shows the variation of χ with respect to α with d and s fixed for the two methods. For both methods the first and second peaks of χ happen near upwave $\alpha = 224°$ (close to the upwind direction $\alpha_w = 213°$) and downwave directions, respectively, while in directions close to the crosswind direction, the value of χ is lower. Figure 10b plots the values of χ for different d with α and s fixed for the two methods. From this figure we see that the fidelity of reconstruction is best around the middle range ($d = 0.5$).

Figure 10c shows the dependence of χ on s with α and d fixed. Although s is usually determined by practical need, the dependence of χ on s is still heuristic. Because of the devolution of the wave field in $\mathscr{D}_1$ with (slow) time as waves (captured in $\mathscr{D}_0$) entering and leaving this subdomain, the correlation $\mathrm{Cor}(\tau)$ between reconstructed and simulated wave fields decreases (slowly) with τ. As expected, χ is better with increasing s for both methods because more waves are captured in $\mathscr{D}_1$. This is so up to a point $s \sim 0.55$ and then χ drops slightly as the boundary of $\mathscr{D}_1$ approaches the radar image center, where the nonuniformity of the radar image intensity is most significant.

Figure 10 suggests that in general, it is more desirable to choose $\mathscr{D}_1$ around an upwind or downwind direction in the middle range with a relatively large size, where higher reconstruction fidelity will be achieved. In the following we will use $\alpha = \alpha_w$, $d = 0.5$, and $s = 0.5$ for the analysis of the dependence of reconstruction on wave field conditions.

b. Dependence on wave field conditions

So far we have focused on the radar image and reconstruction for the wave field condition at a specific location/time corresponding to Table 1. We now study the performance of the PRSC reconstruction for varying wave field conditions. To do that, we use 15 sets of radar data provided by OceanWaves GmbH (2008) obtained in the North Atlantic over an approximately 2-month period. The range of physical parameters covered by these datasets is given in Table 2.

The key independent measurement is the reference (10-m height) surface wind speed U_w, which ranges from $\sim(5–22)$ m s^{-1} in the datasets considered. Figure 11 plots the square root of the wave radar signal-to-noise
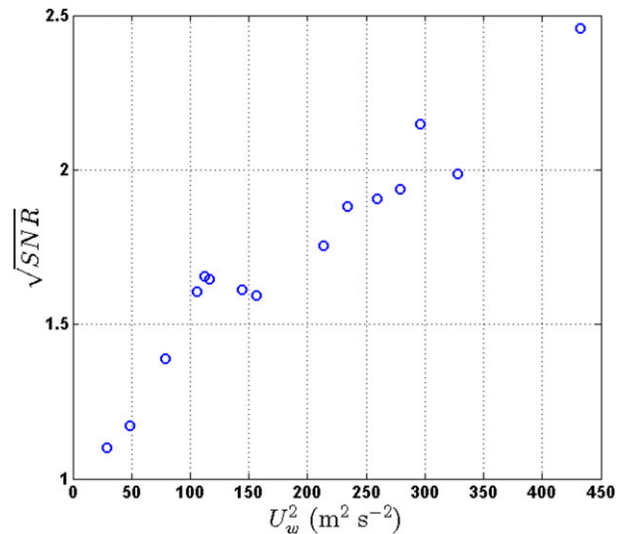

FIG. 11. Variation of $\sqrt{\mathrm{SNR}}$ (using fixed $b = 2$, $c = 2$) with respect to U_w^2 for 15 sets of the radar image sequence. Reconstruction domain is chosen with $\alpha = \alpha_w$, $d = 0.5$, and $s = 0.5$. Raw radar data are provided by OceanWaves GmbH (2008).

ratios $\sqrt{\mathrm{SNR}}$ as a function of U_w^2. As the sea surface roughness increases with U_w, $\sqrt{\mathrm{SNR}}$ increases monotonically and approximately linearly with U_w^2 (with a constant shift). From wave theory (e.g., Bourassa et al. 2001; Sverdrup and Munk 1946, 1947), H_s generally also scales as U_w^2. This supports the linear scaling of H_s with $\sqrt{\mathrm{SNR}}$ in radar reconstruction (Nieto-Borge 1998; Nieto-Borge et al. 2008).

As expected, the optimized reconstruction parameters depend on the wave field conditions, varying appreciably, for example, with wind speed U_w, and using constant reconstruction parameters for sea states is generally inadequate even if for a given radar and fixed reconstruction subdomain.

We first look at the bandpass filter parameter b. Figure 12a shows the variation of χ with respect to b under three different wind speed conditions. We see that in general, χ increases with increasing b because more wave-related signal is retained by the filter until reaching the optimal value b^* and then χ becomes relatively insensitive to b. Under the medium wind condition ($U_w = 10.6$ m s^{-1}), the reconstruction fidelity is generally better than the low or high wind condition. The optimal b is achieved at $b^* = 1.8$ for the medium wind condition, while b^* is 2.1 and 1.2 for the low and high wind conditions, respectively. Figure 12b shows the optimized b^* for all 15 sets of the radar image sequence with different wave field conditions. We see that b^* has a decreasing trend with increasing wind speed U_w for the data we used.

For the shadowing correction parameter q, Fig. 13a shows the variation of χ with respect to q under three
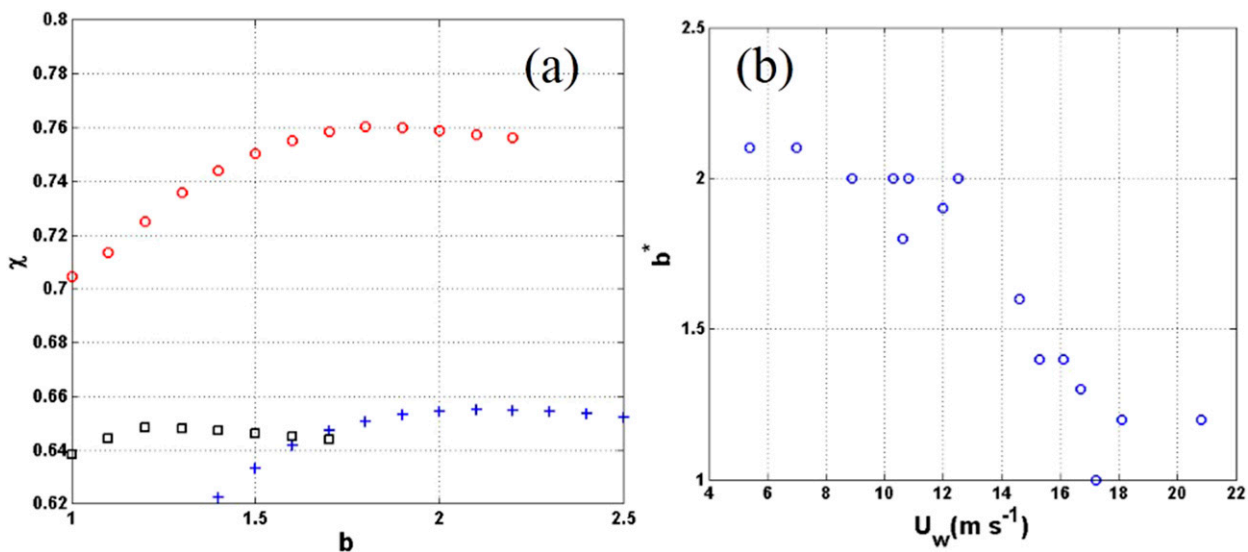
FIG. 12. (a) Variation of χ with respect to b with three different $U_w = 5.4$ (blue plus signs), 10.6 (red circles), and 18.1 m s^{-1} (black squares), with $\alpha = \alpha_w$, $d = 0.5$, $s = 0.5$, and $q = q^*$. (b) Variation of optimized b^* with respect to U_w, with $\alpha = \alpha_w$, $d = 0.5$, $s = 0.5$, and $q = q^*$. The standard method corresponds to fixed $b = 1$. Raw radar data are provided by OceanWaves GmbH (2008).

different wind speed conditions. We see that under medium wind conditions,($U_w = 10.6$ m s^{-1}) the reconstruction fidelity is generally better for different values of q than for the low or high wind condition. The optimal q is achieved at $q^* = 0.5$ for the medium wind condition, while q^* is 0.35 and 1.1 for the low and high wind conditions, respectively. Figure 13b further shows the optimized q^* for all 15 datasets with different wave field conditions. We see that q^* is quite sensitive to U_w. For U_w changing from 5.4 to 20.8 m s^{-1}, q^* varies with a factor up to 4. This figure shows that q^* is positively

correlated to U_w. This is consistent with our finding from Fig. 7c that the shadowing correction exponent increases with increasing H_s/h.

Figure 14 plots the reconstruction fidelity indices χ obtained from the PRSC reconstruction versus that from the standard method as functions of U_w, for a best upwind subdomain. For the standard method, χ varies markedly with U_w, with acceptable results ($\chi \gtrsim 0.5$) only in a relatively limited midrange wind speed of $10 \lesssim U_w \lesssim 16$ m s^{-1}. In contrast, using the PRSC optimized reconstruction, χ is uniformly high over the wind
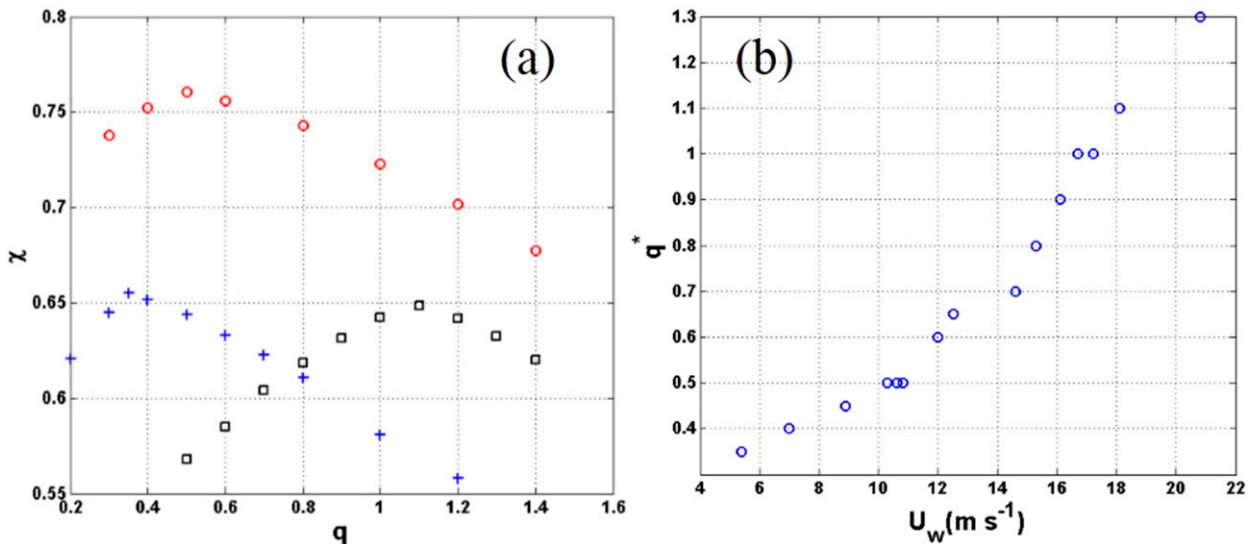

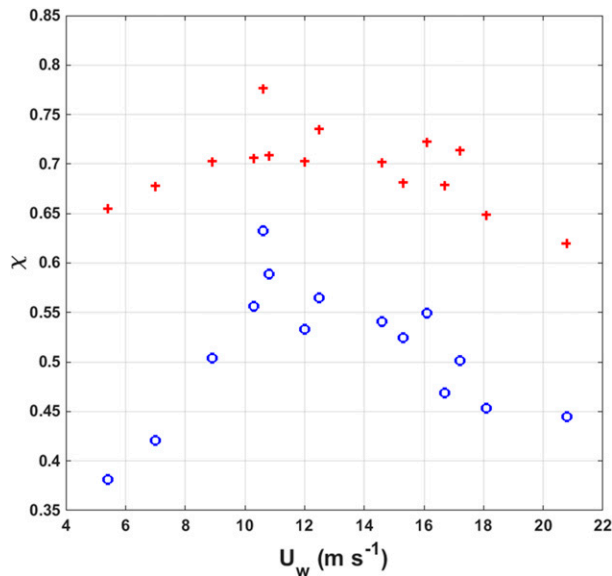FIG. 13. As in Fig. 12, but with respect to q.

FIG. 14. Variation of χ with respect to U_w, where χ is obtained from the PRSC reconstruction (red plus signs) using Π^* (including **U**) and the best subdomain location and size, and from the standard method (blue circles) using Π_0 {with **U** determined by a least squares fit of the dispersion relationship [Eq. (3)]} and the same subdomain. Raw radar data are provided by OceanWaves GmbH (2008).

speeds covered by our dataset ($U_w \in [5.4, 20.8]\,\mathrm{m\,s^{-1}}$). The averaged value across this range is $\overline{\chi} \sim 0.7$ with a standard deviation of only $\sigma_\chi \sim 0.04$. For wind speeds outside the standard method's acceptable range, χ increases significantly (from ~0.35 to ~0.7) with the PRSC method. Even for U_w when the standard method performs best, the PRSC method still increases the reconstruction fidelity appreciably. Thus, the PRSC method substantially expands the range of wave conditions for radar wave reconstruction and increases the reconstruction fidelity.

5. Summary

We propose a phase-resolved simulation calibrated (PRSC) reconstruction method to reconstruct sea surface wave fields from noncoherent X-band marine radar return. Unlike in the existing method, which uses fixed reconstruction parameters, the parameters involved in the PRSC reconstruction are not fixed but assumed to depend on the wave conditions and sampling domain (and slow time). These parameters are optimized to maximize the correlation of the reconstructed wave field and the concurrent phase-resolved simulated wave field, which serves as a metric of the consistency and fidelity of the reconstruction. The standard parameters involved in radar reconstruction are shown, under

PRSC optimization, to vary significantly with the sampling subdomain and sea state, underscoring the inherent difficulties in existing reconstructions using fixed parameters–coefficients. Compared to the latter, the PRSC method produces uniformly and substantially higher consistency and fidelity in the reconstructed wave fields, with the correlation metric increasing by a factor of 2 depending on sea state. Significantly, this higher fidelity is also shown to result in a much broader range of wave conditions, as measured, say, by the surface wind speed. For simplicity, in the present paper, we illustrate the PRSC method and the results for a finite duration (~48 s corresponding to 32 frames of the radar return data), typically $\gtrsim 7T_p$ for all the wave conditions we considered. In practice, with additional–continuous radar data over time, the process we describe is extended in a straight-forward manner, with the reconstruction parameters continually optimized over a moving correlation time window. For illustration, we have used fairly high-quality radar images (from fixed installations) in this paper. In practical applications, the radar return data may be degraded due to physical and nonphysical conditions. In these cases, the optimized reconstruction parameters may not be easy to obtain and/or physically reasonable, and therefore caution is needed in such situations.

REFERENCES

Alam, M., Y. Liu, and D. Yue, 2009: Bragg resonance of waves in a two-layer fluid propagating over bottom ripples. Part II. Numerical simulation. *J. Fluid Mech.*, **624**, 225–253, doi:10.1017/S002211200800548X.

Alpers, W., and K. Hasselmann, 1982: Spectral signal to clutter and thermal noise properties of ocean wave imaging synthetic aperture radars. *Int. J. Remote Sens.*, **3**, 423–446, doi:10.1080/01431168208948413.

Bourassa, M., D. Vincent, and W. Wood, 2001: A sea state parameterization with nonarbitrary wave age applicable to low and moderate wind speeds. *J. Phys. Oceanogr.*, **31**, 2840–2851, doi:10.1175/1520-0485(2001)031<2840:ASSPWN>2.0.CO;2.

Dankert, H., and W. Rosenthal, 2004: Ocean surface determination from X-band radar-image sequences. *J. Geophys. Res.*, **109**, C04016, doi:10.1029/2003JC002130.

Dommermuth, D., and D. Yue, 1987: A high-order spectral method for the study of nonlinear gravity waves. *J. Fluid Mech.*, **184**, 267–288, doi:10.1017/S002211208700288X.

——, and ——, 1988: The nonlinear three-dimensional waves generated by a forward-moving surface disturbance. *17th Symposium on Naval Hydrodynamics*, National Academy Press, 523–542.

Hasselmann, K., and Coauthors, 1973: Measurements of wind-wave growth and swell decay during the Joint North Sea Wave Project (JONSWAP). Deutschen Hydrographischen Institut Ergänzungsheft 8-12, 95 pp.

Lee, P., and Coauthors, 1995: X band microwave backscattering from ocean waves. *J. Geophys. Res.*, **100**, 2591–2611, doi:10.1029/94JC02741.

Liu, Y., and D. Yue, 1998: On generalized Bragg scattering of surface wave by bottom ripples. *J. Fluid Mech.*, **356**, 297–326, doi:10.1017/S0022112097007969.

Mei, C., M. Stiassnie, and D. Yue, 2005: *Theory and Applications of Ocean Surface Waves*. Advanced Series on Ocean Engineering, Vol. 23, World Scientific, 1136 pp.

Nieto-Borge, J., 1998: Significant wave height estimation from nautical radar data sets. GKSS Research Center Geesthacht Rep. 98/E/28, 34 pp.

——, G. Rodrguez, K. Hessner, and P. Izquierdo, 2004: Inversion of marine radar images for surface wave analysis. *J. Atmos. Oceanic Technol.*, **21**, 1291–1300, doi:10.1175/1520-0426(2004)021<1291:IOMRIF>2.0.CO;2.

——, K. Hessner, P. Jarabo-Amores, and D. de la Mata-Moya, 2008: Signal-to-noise ratio analysis to estimate ocean wave heights from X-band marine radar image time series. *IET Radar Sonar Navig.*, **2**, 35–41, doi:10.1049/iet-rsn:20070027.

OceanWaves GmbH, 2008: Raw data of X-band marine radar measurements at North Atlantic Ocean in 2006 and 2007. OceanWaves GmbH, accessed 11 May 2016. [Available online at http://web.mit.edu/vfrl/www/research/Yusheng/Data/RadarData.html.]

Plant, W., and W. Keller, 1990: Evidence of Bragg scattering in microwave Doppler spectra of sea return. *J. Geophys. Res.*, **95**, 16 299–16 310, doi:10.1029/JC095iC09p16299.

——, and L. Zurk, 1997: Dominant wave directions and significant wave heights from synthetic aperture radar imagery of the ocean. *J. Geophys. Res.*, **102**, 3473–3482, doi:10.1029/96JC03674.

Seemann, J., F. Ziemer, and C. Senet, 1997: A method for computing calibrated ocean wave spectra from measurements with a nautical X-band radar. *Oceans'97: MTS/IEEE Conference Proceedings*, Vol. 2, IEEE, 1148–1154, doi:10.1109/OCEANS.1997.624154.

Sverdrup, H., and W. Munk, 1946: Empirical and theoretical relations between wind, sea and swell. *Trans. Amer. Geophys. Union*, **27**, 823–827, doi:10.1029/TR027i006p00823.

——, and ——, 1947: Wind, sea and swell: Theory of relations for forecasting. U.S. Hydrographic Office Tech. Rep. 1, H. O. Publ. 601, Scripps Institution of Oceanography 303, U.S. Navy, 60 pp.

Valenzuela, G., 1978: Theories for the interaction of electromagnetic and oceanic waves—A review. *Bound.-Layer Meteor.*, **13**, 61–85, doi:10.1007/BF00913863.

Young, I., W. Rosenthal, and F. Ziemer, 1985: A three-dimensional analysis of marine radar images for the determination of ocean wave directionality and surface currents. *J. Geophys. Res.*, **90**, 1049–1059, doi:10.1029/JC090iC01p01049.

Ziemer, F., and H. Gűnther, 1994: A system to monitor ocean wave fields. Preprints, *Second Int. Conf. on Air–Sea Interaction and Meteorology and Oceanography of the Coastal Zone*, Lisbon, Portugal, Amer. Meteor. Soc., 18–19.